EFFECT OF LITHIATION UPON THE SHEAR STRENGTH OF NMC811 SINGLE CRYSTALS

J.C. Stallard[1,2], S. Vema[2,3], D. Hall[2,3], A.R. Dennis[1], M. Penrod[2,3], C.P. Grey[2,3], V.S. Deshpande[1,2], N.A. Fleck[1,2]

ABSTRACT

An experimental protocol is developed to measure the shear strength of NMC811 single crystals within the cathode of a lithium-ion cell. The cathode is placed upon a set of thick metallic substrates that possess a wide range of indentation hardness. For each choice of substrate, the top surface of the cathode is indented by a Vickers indenter to a sufficient depth that the cathode layer is subjected to an approximately spatially uniform compressive normal traction equal to the hardness of the substrate. The sensitivity of plastic flow and fracture of the single crystals to substrate hardness is determined by observation of the particles in the indented top surface of the cathode using a scanning electron microscope. It is found that the shear strength of fully lithiated, as-manufactured NMC811 single crystals along their basal plane is of order 80-90 MPa, and decreases upon cell charging (delithiation of the cathode). This implies that particle slip and fracture will occur under mild mechanical loading, for example by calendering during manufacture and by electrical cycling of the compacted cathode. The indentation protocol developed here has application to a wide range of single crystal cathode materials.

[1] Department of Engineering, University of Cambridge, Trumpington St., CB2 1PZ, UK.
[2] The Faraday Institution, Quad One, Bacquerel Ave, Harwell Campus, Didcot, OX11 0RA, UK
[3] Department of Chemistry, University of Cambridge, Lensfield Rd., Cambridge, CB2 1EW, UK.

1. INTRODUCTION

Layered oxides of composition $Li_yNi_xMn_zCo_{(1-x-z)}O_2$, (NMC), in which the lithium content y varies in the range $0 < y < 1$, are widely used as the active storage material in lithium ion battery (LIB) cathodes [1,2]. Typically, NMC cathodes are manufactured by the tape-casting of a solvent-based slurry of NMC particles, polymeric matrix and carbon powder onto an aluminium film, which serves as a current collector [3]. Evaporation of the solvent leaves a porous cathode microstructure, with typical volume fraction of active storage material (in the pre-compacted state) between 0.40 and 0.60, and carbon-infiltrated polymer of volume fraction less than 0.1. The remaining 30% to 50% of the cathode volume is porosity [3,4].

A calendering operation is often used to increase the particle packing density (and reduce the porosity) of the cathode. This reduces both cell volume and cell mass (by reducing the amount of encapsulation), and thereby increases the storage energy and the power capacity of the cell, per unit volume and per unit cell mass. Computed tomography (CT) studies of cathodes that comprise polycrystalline NMC particles have reported that the calendering operation can lead to significant particle fracture and pulverisation [5,6]. For typical NMC cathodes, the increase in achievable charging rate after calendering is ascribed to an enhanced effective electrical conductivity of the cathode composite [3,7-9]. Calendering helps to reduce interfacial resistance between active material and current collector and hold the whole structure together during extended cycling.

The need to extend cycle life of NMC cathodes has led to the recent development of so-called single crystal cathodes, whereby NMC particles comprise single domain, micron-sized particles (and bi-crystals) [10,11]. Previously, NMC cathode material existed in the form

of *primary* particles of diameter between 0.1 µm and 1 µm, agglomerated into polycrystalline *secondary* particles of diameter between 3 µm and 20 µm [12-15]. These secondary particles suffer from the drawback that lithiation and delithiation induce intergranular fracture between the primary grains. Intercalation of Li ions induces anisotropic swelling within each primary grain, and the elastic constraint imposed by neighbouring primary grains leads to stressing of the grains and of the grain boundaries. These self-equilibrating stresses may be of sufficient magnitude to induce fracture of the grain boundaries between primary grains over a charge cycle [16]. In contrast, much lower stresses are generated in single crystal cathodes due to the reduced elastic constraint between neighbouring single crystals. This might be the reason that single crystal cathodes have exceptional resistance to degradation [17], retaining over 90% of their initial capacity over 4 000 full cycles.

A typical single crystal of NMC811 is sketched in Fig. 1a. It has the $R\bar{3}m$ space group, and exists as a single phase. The prismatic direction is denoted by the unit vector $\boldsymbol{c}$. The mutually orthogonal $\boldsymbol{a}$ and $\boldsymbol{b}$ lattice directions of the basal plane sit in the prismatic plane of the particle. Thus, the orthonormal vectors $(\boldsymbol{a}, \boldsymbol{b}, \boldsymbol{c})$ are aligned with the principal directions of the lattice. It is generally recognised that the unit cell dimensions of NMC811 are sensitive to the state of charge. The lattice parameters a and c are plotted against lithium occupancy y in Fig. 1b [18]; both a and c are normalised by their values in a fully lithiated state, as denoted by a_0 and c_0. There is no need to consider the third lattice constant b as $b/b_0 = a/a_0$ in the basal plane of the unit cell. During delithiation (decreasing y), c/c_0 initially rises, and then subsequently falls for $y < 0.3$, whereas a/a_0 decreases with decreasing y.

The mechanical properties of NMC single crystals have not been reported in the open literature to the best of the authors' knowledge. Single pillar compression experiments have

been performed on other layered oxides such as Li_yCoO_2 (LCO). For example, Feng *et al*. [19] have found that the uniaxial compressive strength of an isolated LCO crystal is on the order of 2-4 GPa in the initial, uncycled state. They observed two deformation modes of the pristine LCO: (i) a shear mode on an inclined plane at an axial stress of 2 GPa, see their Fig. 4b; and (ii) uniform plastic straining by dislocation-mediated plasticity, at an axial stress of 4 GPa, see their Fig. 4a. A *possible* interpretation for these modes is that plastic deformation may occur via two mechanisms, as follows:

Mechanism (i). Single slip occurs on the prismatic plane of the layered oxide when the critically-resolved shear stress on a slip plane, inclined to the loading axis in a single pillar test, attains a value on the order of 100 MPa, corresponding to an axial stress of 2 GPa. Feng et al [19] refer to this inclined plane as a 'cleavage plane' rather than a slip plane. This motivates the present study: does single slip occur in layered oxides at values of shear stress on the order of tens or hundreds of MPa rather than several GPa? Such slip at low resolved shear stress is consistent with recent observations and calculations for NMC811 single-crystal cathodes under cyclic electrical loading [20]: slip bands were observed in NMC811 single crystals under electrochemical cycling, and the predicted shear stresses within the crystals due to charge and discharge did not exceed a few hundred MPa.

Mechanism (ii). Additional, secondary slip systems can be envisaged, but these slip systems will be much stronger than the primary slip system on the basal plane; activation of several of these additional slip systems gives rise to uniform plastic straining by dislocation-mediated plasticity. The results of Feng *et al*. [19] suggest that this occurs at an axial stress of 4 GPa.

The measured indentation hardness of polycrystalline NMC secondary particles is in the range 5-8 GPa [15,21], but it is a challenge to relate this macroscopic quantity to the shear

strength of the primary grains. The usual interpretation that the macroscopic hardness of a polycrystal equals three times its uniaxial strength is only valid for a crystal that possesses at least 5 slip systems [22]. Layered polycrystalline ceramics have a much-reduced availability of slip systems, and consequently their macroscopic hardness may be dictated by the activation of secondary slip systems of slip strength much above that of the basal plane, or by the granular flow of the polycrystalline ceramic after it has suffered extensive fragmentation along its grain boundaries.

Scope of Study

In the present study, an indentation-based test protocol is developed to measure the basal shear strength of a large number of fully lithiated (y = 1) NMC811 single crystals in-situ within a cathode layer. The imposed compressive stress on the NMC single crystals is set by the indentation hardness of the underlying metallic substrate, and the number fraction of single crystals that have undergone plastic slip and fracture is observed post-indentation. The test procedure is then used to determine the sensitivity of the NMC811 single crystal strength to lithium occupancy y, by repeating the experiments on cathodes that have been extracted from Li ion cells in various states of charge.

2. TEST PROTOCOL: INDENTATION OF AN NMC811 CATHODE UPON A SUBSTRATE OF DEFINED HARDNESS

a. Test Material

NMC811 cathodes[4] comprise a porous microstructure in the tape cast but uncalendered state. The cathode active material is cast upon the current collector at an areal density of 0.167 kg m^{-2}. The as-received, fully lithiated (y = 1) cathode and aluminium backing are of thickness 65 μm and 15 μm respectively, as measured by CT scanning[5]. Upon taking the density of $LiNi_{0.8}Mn_{0.1}Co_{0.1}O_2$ as 4780 kg m^{-3} [23,24] it follows that the NMC cathode particles comprise 54% of the cathode volume; the remainder is 7% graphite-infiltrated polymer binder, and 39% porosity, which allows for infiltration by a liquid electrolyte. A plan view of the cathode microstructure is shown in Fig. 2a, as observed in a scanning electron microscope[6] (SEM). Many of the particles are prismatic in shape and it is assumed that the *c*-axis of the layered crystals is aligned with the prismatic direction.

The SEM images of the fully lithiated (y = 1) cathode microstructure reveal that most of the single crystal particles have a diameter in the range 1 μm to 3 μm. A small proportion of them contain slip bands or multiple fractures in the pristine state, examples of which are shown in Figs. 2b and 2c, respectively. The proportion of cathode particles with slip bands and fractures was measured by obtaining ten SEM images of the cathode microstructure at a fixed magnification of ×10^4: each image contained about 100 particles. From these images, an average number fraction of 0.88 of the particles contain neither slip bands nor cracks. The number fraction with slip bands, but no indication of fracture, was 0.11, and the remaining number fraction of particles (<0.01) had either single or multiple fractures, or a combination of fractures and slip bands.

---

[4] Li-FUN Technology Corporation Ltd., Block J, Taynes Science Park, No. 128 Chuangye Av., Tianyuan District, Zhuzhou City, Hunan Province, P.R. China.
[5] Zeiss Xradia 520 Versa CT Scanner. Zeiss Ltd., Zeiss House, Building 1030, Cambourne Business Park, Cambourne, Cambridge, CB23 6DW, United Kingdom.
[6] Tescan MIRA3 FEG-SEM. TESCAN-UK Ltd., Wellbrook Court, Girton, Cambridge, CB3 0NA, United Kingdom.

The lithium content y of the NMC was varied by assembling Li-ion cells, using the as-received cathode, a graphite anode, and a liquid electrolyte; full details are reported in a previous study [18]. In brief, additional values of $y = 0.58$ and $y = 0.14$ were achieved as follows. A charging current of 1/20th of the full cell charge capacity per hour (C/20) was used until cell voltages of 3.8 V and 4.4 V were obtained, which correspond to $y = 0.58$ and $y = 0.14$ respectively [18]. These two values of voltage were held fixed for 20 hours, after which the cells were disconnected and disassembled, all within a sealed glovebox under an argon atmosphere. The electrolyte was removed by rinsing the cathodes with dimethyl carbonate, followed by drying under vacuum. We shall subsequently show that this procedure, involving a low charging current to delithiate the cathode, does not change the number fraction of slipped and fractured grains prior to the indentation tests.

b. Indentation tests

The indentation method used in this study to measure the yield and fracture response of single crystal NMC811 particles is now discussed. Particles within the cathode were subjected to a macroscopic uniform compressive stress, as dictated by the indentation hardness of the chosen substrates. The hardness was varied by a factor of almost 20 by suitable choice of substrate, from annealed lead to work-hardened copper. It is assumed that slip or fracture of any particle occurs when the resolved shear stress on the basal slip plane of that particle attains a critical value. A mechanics analysis is used to determine the value of this critically resolved shear stress, and to estimate the distribution function of particle orientation. The details are given below.

The stress field created by indentation of an elastic, ideally plastic solid by a Vickers indenter, with a surface layer absent, has already been detailed by finite element simulations [25,26]. It is found that the compressive traction along the flanks of the indenter is almost uniform in space, and of magnitude about three times the uniaxial yield strength of the substrate. A small elevation in traction occurs at the tip of the indenter [27] and along the sharp edges between the facets [28] but their effects upon the indenter load is negligible [25-28]. If a thin film exists between the substrate and the indentation tip, and the indentation depth is much greater than the film thickness, then the indentation pressure is hardly perturbed by the presence of the thin film [29,30]. In the current study, the indentation depth was 2-3 times that of the coating thickness. Preliminary experiments revealed that the observed hardness is independent of indent depth provided the indent depth exceeded 1.5 times the coating thickness. Also, no delamination was observed beneath the indenter. The significance of pile-up versus sink-in is accounted for by making visual observation of the projected area of indent.

In a preliminary set of tests with two extremes of substrate hardness (Hv ? and Hv?), a set of 10 indents were made at fixed indentation load. The projected area of each residual indent was measured and it was found to vary by at most 5% about the mean value. This confirmed that the cathode material was uniform in properties. The number fraction of slipped and fractured particles was also measured for each indent, and was again found to be constant (to within +-5%). The number of particles examined over the indent area was of the order of 400 per indent. Once these checks had been made, a single indent was studied for each choice of substrate.

Conical indentation has the advantage that the indenter has no intrinsic length scale, only a characteristic angle of indenter, see for example Johnson (). Consequently, the strain state of a semi-infinite solid indented by a conical indenter immediately achieves a steady state that depends only upon Cartesian co-ordinate *x* of a material point normalised by the

current contact radius a. The strain field is of finite magnitude except in a small region in the vicinity of the conical tip. In contrast, a flat bottomed indenter (such as a frictionless circular punch) as a characteristic length scale of the punch radius. Further, a singular stain state exists at the edge of contact which is identical to that of crack singularity. The magnitude of this strain singularity will increase with indentation depth. Likewise, the strain at any pint beneath the punch will increase with increasing indentation depth, and so a steady state is not achieved.

A series of indentation tests were performed with the cathode supported by flat, polished metal substrates of thickness 6 mm or greater. The tests were performed using a Vickers diamond indentation tip[7] affixed to the crosshead of a screw-drive mechanical test machine[8]. The test machine and indentation experiments were performed in an inert argon gas atmosphere within a glovebox[9], in which the concentrations of oxygen and water were both maintained at less than 0.1 ppm.

The diamond Vickers tip has the shape of a square pyramid, in which the four triangular facets are inclined at an angle of 22° from the base, and the tip radius equals 2 μm. The indentation tests were performed at a velocity of 2 μm s^{-1} until a specified indentation load P_I was obtained; the tip was then withdrawn from the sample. Indents were made at loads P_I in the range 25 N $\leq P_I \leq$ 520 N, depending upon the hardness of the substrate: higher indentation loads were imposed on cathodes that rested on harder substrates to

---

ensure that the indent displacement was always much greater than the thickness of the cathode, and that all indents were of approximately equal area.

The hardness of the metallic substrates was varied from 50 MPa to 946 MPa by a suitable selection of metals and alloys including lead, tin solder, aluminium and copper, and subjecting them to various heat treatments and work hardening treatments. Details of the alloys, their composition, heat treatment, and work hardening treatment are listed in Table S1 of the supplementary information, along with their measured hardness H absent a cathode layer: H equals the indentation pressure on the as-measured projected area of indent A_P, and is related to the indentation load P_I by $H = P_I/A_P$.

c. Deformation of cathode due to indentation

An image of a representative indent in a fully lithiated (y = 1) cathode is shown in Fig. 3a, for an annealed aluminium substrate of hardness $H = 179$ MPa and an indentation load $P_I = 120$ N. The thickness profile of the cathode during indentation was obtained by making use of a custom-built, in-situ indentation rig inside a CT scanner. Sufficient X-ray penetration for practical imaging was achieved at an acceleration voltage of 80 kV by employing a polished annealed aluminium cylinder of diameter 10 mm as the substrate. A computed tomography scan of the cross-section of the cathode during indentation is shown in Fig. 3b at an indent load of 120 N. The section is made on plane A-A, as defined in the SEM top view of the indented cathode surface in Fig. 3a. The thickness h is plotted against distance s from the indenter apex in Fig. 3c, and the interpretation of the deformation state of the cathode layer, sandwiched between the indenter and the substrate, is given in Fig. 3d. When the indentation depth of the Vickers indenter exceeds twice the cathode thickness, the

average normal compressive traction on the layer in contact with the indenter is close to that of the substrate hardness H [29]. This is confirmed by the accompanying observation that the indent size of the substrate beneath the cathode layer is close to the indent size for indentation of the substrate alone at an identical load.

Post-indentation SEM imaging of the compressed microstructure of the fully lithiated cathode is shown in Fig. 4a due to the indentation performed as reported in Fig. 3. The degree of compaction of the cathode layer varies from high compaction at the apex, to a uniform state of moderate compaction along the flanks, to a low degree of compaction at the periphery of the indent. No compaction was evident in the pristine cathode material external to the indent. Examples of individual particles with signs of plastic deformation are shown in Figs. 4b-4d. The particles may display slip bands alone (Fig. 4b), or may display a combination of slip bands and cracks (Figs. 4c and 4d).

Confirmation that the substrate hardness dictates the compressive stress to which a cathode is subjected in indentation testing is illustrated by images of indented, fully lithiated cathode microstructure, as shown in Fig. 5. All images were obtained at a radial distance $\sqrt{A_P}/4$ from the apex of each indent, which is approximately mid-way along the tip flanks of uniform compaction pressure zone as identified in Fig. 3d. The degree of compaction in the cathode microstructure at this location increases with increasing substrate hardness H.

d. The number fraction of single crystals that yield and/or fracture as a function of indentation pressure

The effect of the level of pressure on the active material particles was assessed by imaging the microstructure of the indented cathode at a radial distance $\sqrt{A_P}/4$ from the apex of the indent. From these images, the number fraction of particles that possess slip bands, or various combinations of fractures and/or slip bands, was measured by particle counting. All images were obtained using the same magnification of $\times 10^4$ as that employed for assessing the fraction particles with slip bands or fractures in the pristine cathode. The fraction of slipped and fractured particles counted from indented cathodes are plotted in Figs. 6a-6c, against the hardness of the metal substrate, for cathodes in a fully lithiated state (for which $y = 1$), and two other states of charge, $y = 0.58$ and $y = 0.14$. The value $y = 0.58$ is not at the peak value of c/c_0 but does give rise to a noticeably expanded c lattice parameter whereas the value $y = 0.14$ is close to the fully delithiated state. The cell potential, along with the states of $y = 1$, 0.58 and 0.14, are included in Fig 1b; the cell potential rises as the lithium occupancy y decreases during cell charge.

For all cathodes ($y = 0.14, 0.58$ and 1), the number fraction of particles that display both slip and fracture increase with increasing pressure (as defined by the hardness of the substrate). In the case of the fully lithiated ($y = 1$) particles (Fig. 6a), the fraction of particles that possess slip bands alone initially rises with indentation pressure, up to a pressure of approximately 400 MPa. This number fraction then decreases under increased indentation pressure, as many of the slipped particles proceed to fracture. A negligible proportion of particles crack without slip. The slip plane is always parallel to the prismatic direction – that is parallel to the basal plane of the layered lattice.

A close connection between yield and fracture of the particles is evident, and consequently we introduce the number fraction F of particles that have slipped and/or

fractured and write F as a function of hardness H. The observed response $F(H)$ is plotted in Fig. 7 for $y = 0.14, 0.58$ and 1. For all three states of lithiation y, F equals an initial value $F_0 = 0.12$ in the pristine state to within experimental scatter, confirming that charging the cell at C/20 does not induce fracture/slip in the NMC crystals. The number fraction F is maintained at $F = F_0$ as H is increased up to a threshold value H_0, and then F increases sharply for $H > H_0$. Note from Fig. 7 that the value of H_0 is sensitive to the value of y, such that $H_0 = 93$ MPa, 51 MPa and 42 MPa respectively. It is also noted that the dependence of F upon H/H_0 is independent of the lithiation state y; see Fig. 7b. This observation helps motivate a mechanics model to explain the micromechanical origins of $F(H/H_0)$ as detailed in the following section.

3. AN ESTIMATION OF BASAL PLANE SHEAR STRENGTH

It remains to relate the average compressive traction (which equals the substrate hardness H) on the surface of the cathode layer to the shear stress on the crystallographic basal plane within the cathode particles. The cathode microstructure and stresses within it are sketched in Fig. 8a. The simplest approach is to employ the Reuss lower bound assumption such that the uniaxial stress σ within each crystal is related to the substrate hardness H and cathode porosity f according to

$$\sigma = H/(1 - f) \qquad (1)$$

The porosity of the uncalendered material is $f = 0.46$ upon treating both the 7% carbon-infiltrated polymer binder, and the 39% air as porosity. The resolved shear stress τ on

any basal plane, with unit normal $\boldsymbol{c}$ inclined at an angle ϕ to the loading direction (defined in Fig. 8b is related to the hardness H via

$$\tau = \frac{H \sin 2\phi}{2(1-f)} \tag{2}$$

Consequently, the resolved shear stress τ vanishes for $\phi = 0, \pi/2$ for any finite value of H. Between these limits, τ rises towards a maximum value $\tau^{\max}$ at a basal plane inclination of $\phi = \pi/4$.

The hardness H_0 is defined as that which gives $\tau^{\max} = \tau_C$, where τ_C is the shear strength of the basal plane. From (2) it follows that the value of hardness $H_0 = 2(1-f)\tau_C$ initiates yield of the most favourably oriented particles. It is further assumed that the degree of slip on the basal plane is limited by jamming of the slipped particle against its neighbours, so that, post-yield, the particle can bear a shear stress on the basal plane that exceeds τ_C. Recall that we make no distinction between yield or fracture of a particle and simply refer to a particle as either "slipped" or "unslipped".

Now consider the application of a pressure $H > H_0$. Then, all particles of orientation ϕ in the range $\phi_L < \phi < \phi_U$ will slip, where $\phi_L < \pi/4 < \phi_U$. The values of ϕ_L and ϕ_U are the two solutions for which $\tau = \tau_C$. The roots of (2) are symmetric about $\phi = \pi/4$ such that $\phi_L + \phi_U = \pi/2$; the larger root is denoted by ϕ_U and satisfies

$$\sin 2\phi_U = \frac{2(1-f)\tau_C}{H} = \frac{H_0}{H} \tag{3}$$

The lattice orientation of the basal plane of each particle, as defined by the unit normal $\boldsymbol{c}$, can be written in terms of the spherical co-ordinates (ϕ, θ), as sketched in Fig. 8b. Consider the probability distribution function $p(\boldsymbol{c})$ of the unit normal $\boldsymbol{c}$ over a sphere of unit area S,

(and of radius $r = 1/(2\sqrt{\pi})$). For any suitably normalised probability density function $p(c)$, its integration over unit surface S equals unity,

$$\int_S p(c)ds = 1. \tag{4}$$

Assume that the orientation of particles within the cathode is transversely isotropic within the plane of the cathode as a result of the deposition process of the crystals during manufacture, such that $p(c)$ is independent of θ (Fig. 8b) and can thereby be written as $p(\phi)$. The cumulative number fraction F of slipped particles at any value of applied uniaxial stress σ is given by

$$F - F_0 = (1 - F_0) \int_{\frac{\pi}{2} - \phi_U}^{\phi_U} p(\phi) \sin \phi \, d\phi, \tag{5}$$

where F_0 is the fraction of slipped particles in the initial pristine state. The indentation results of the present study can be used deliver the curve $F(H)$, upon noting that σ is directly related to H via (1).

The challenge is to obtain the probability curve $p(\phi)$ from $F(H)$ by suitable inversion of (5). To do so, the simplest approach is to first generate an analytical form for $F(H)$ by a curve fit to the measured response for $F(H)$, for any value of lithiation y. Suitable agreement with experiment is obtained upon assuming that the plots of $F(H)$ versus H/H_0 in Figs. 7a and 7b satisfy the curve fit

$$F - F_0 = (1 - F_0)\left[1 - \left(\frac{\frac{H}{H_0} - \alpha}{1 - \alpha}\right)^2\right]^{\frac{1}{2}} \tag{6}$$

15

Here, H_0 is the value of substrate hardness that first initiates slip (or fracture) and is dependent upon the degree of lithiation y; $\alpha > 1$ is a fitting parameter with the interpretation that $F = 1$ when $H/H_0 = \alpha$. A best fit gives $\alpha = 20$ for all values of y, and $H_0 = 93$ MPa, 51 MPa and 42 MPa for $y = 1$, 0.58 and 0.14, respectively. The derivative $F'(H)$ follows from (6) as

$$F'(H) = \frac{(1 - F_0)\left(\alpha - \frac{H}{H_0}\right)}{H_0(1 - \alpha)^2}\left[1 - \left(\frac{\frac{H}{H_0} - \alpha}{1 - \alpha}\right)^2\right]^{-\frac{1}{2}} \tag{7}$$

while $F'(H)$ follows from (5) as

$$F'(H) = \left[p(\phi_U)\sin\phi_U + p\left(\frac{\pi}{2} - \phi_U\right)\sin\left(\frac{\pi}{2} - \phi_U\right)\right]\frac{d\phi_U}{dH}. \tag{8}$$

The derivative $d\phi_U/dF$ is obatined by differentiating (3) with respect to H such that

$$(2\cos 2\phi_U)\frac{d\phi_U}{dH} = -\frac{H_0}{H^2} = -\frac{\sin 2\phi_U}{H}. \tag{9}$$

Upon equating (7) and (8) and assuming that $p(\phi_L) = p(\phi_U)$, we obtain

$$p(\phi_U) = \frac{2(1 - F_0)\frac{H}{H_0}\left(\frac{H}{H_0} - \alpha\right)}{(1 - \alpha)[\sin\phi_U + \cos\phi_U]}\left[\frac{\left(\frac{H}{H_0}\right)^2 - 1}{(1 - \alpha)^2 - \left(\frac{H}{H_0} - \alpha\right)^2}\right]^{\frac{1}{2}} \tag{10}$$

upon making use of (3) and (9). For any given value $1 \le (H/H_0) \le \alpha$, the corresponding value of ϕ_U follows from (3), and the value of $p(\phi_U)$ follows immediately from (10).

The single value for α provides a suitable fit for all lithiation states (Fig. 7b), consistent with our expectation that the orientation of particles within a cathode is unchanged by the

degree of cathode charge. The inferred shear strength τ_C is plotted against the degree of lithiation y in Fig. 7c, and the distribution of basal plane orientation of particles $p(\phi)$ as deduced from (10) is plotted in Fig. 7d. Some limiting cases provide insight into this predicted distribution. From (10), $p(\pi/4)$ equals $(1 - F_0)\sqrt{2/(\alpha - 1)}$ and it is this fraction of particles that first slip at $H = H_0$. Also, note that the choice (6) of curve fit states that all crystals have slipped, $F = 1$, at a finite value of pressure, $H/H_0 = \alpha$. Consequently, $p(\phi)$ vanishes over the small intervals $0 \le \phi \le \phi_L$ and $\phi_U \le \phi \le \pi/2$ where $\phi_L \approx (1/\alpha)$ and $\phi_U \approx \pi/2 - (1/\alpha)$ via (3). It is worth mentioning in passing that measured data only extends to $H/H_0 \approx 10 = \alpha/2$ (Fig. 7b) and thus there is some uncertainty in our estimation of $p(\phi)$ around $\phi = \phi_L$ and ϕ_U. However, with $\alpha = 20$, $\phi_L \approx 0$ and $\phi_U \approx \pi/2$ this interval of uncertainty is small and therefore does not represent a major drawback to this method as a means of extracting the shear strength of the crystals.

A shear strength τ_C of the basal plane in the range 39 MPa to 86 MPa is several orders of magnitude below the measured Vickers hardness of polycrystalline NMC secondary particles [15, 20]. This apparent discrepancy is reconciled by recognising that other ceramic materials, whose atomic structure is similarly layered such as MAX phase compounds, also exhibit shear strengths of their basal plane that are much below both the measured hardness and compressive strength of polycrystalline samples [31]. For example, for the case of Ti_3SiC_2, the critical resolved shear stress required to activate slip on the basal plane is 16.5 MPa [32]. In contrast, the compressive strength of Ti_3SiC_2 crystals when loaded in a direction within the basal plane is approximately 4 GPa [32], and is due to kinking of the lattice layers due to the low shear strength between them. The compressive strength of fine-grained Ti_3SiC_2 exceeds 1 GPa [31], which is some 60 times the shear strength of the basal plane. In the case of

polycrystalline NMC samples, the constraints imposed by neighbouring grains preclude their deformation in hardness testing by basal slip alone. General yield requires slip on at least 5 independent slip systems, and a high yield strength of the required secondary slip systems results in a hardness (and uniaxial compressive strength) much above that of the basal plane shear strength.

The shear strength τ_C drops rapidly as the Li$^+$ ions are removed from the structure and the c-parameter (and thus interlayer spacing) expands from a Li content of $y = 1$ to 0.58, recall Fig. 1b. A smaller change in τ_C results from additional removal of Li (from $y = 0.58$ to 0.14), presumably because the interlayer spacing decreases noticeably beyond $y = 0.35$, approximately.

The cathode layer of the present study is in the uncalendared state, as is evident by its high porosity. Indentation of the thin uncalendared cathode layer by the Vickers indenter subjects the layer to normal stress that is sufficiently large that the coating compresses by a large strain in the normal direction, and a small transverse strain. The precise stress state depends upon the compaction response of the powder aggregate, and this is unknown for the cathode layer. The simplest idealisation is adopted here, that the 'plastic Poisson ratio' is close to zero and so uniaxial stress generates uniaxial strain. This is reasonable approximation for low density aggregates such as a metallic foam, where a state of uniaxial compressive stress generates a state of uniaxial compressive strain, see for example Deshpande and Fleck (2000). We further note that the assumption of a state of uniaxial compression with vanishing transverse stress leads to a predicted single crystal strength that exceeds the value that would be obtained for the case of a finite compressive transverse stress in the cathode layer. In this sense, the single crystal shear strengths of the present study are upper estimates of the actual values.

4. CONCLUSIONS

An indentation-based test method has been developed to determine the slip strength of NMC811 single crystals within a porous cathode. The level of imposed compressive stress upon the cathode is dictated by the substrate hardness. By measuring the number fraction of single crystals with visible signs of plastic flow (and/or fracture) as a function of substrate hardness, the compressive stress needed to active plastic flow of the single crystals within the cathode was determined. The resolved shear strength of the single crystals was deduced from this normal stress, and was found to be 86 MPa in the pristine state of a fully lithiated cathode, decreasing to 39 MPa upon delithiation (associated with cell charging and loss of the Li^+ ions which hold the negatively charged metal oxide layers of the cathode together). This low strength suggests that fracture or plastic slip of the NMC811 single crystals might occur because of mild mechanical loading (e.g., via a calendaring operation) or due to mechanical loads generated during electrical cycling of a compacted cathode.

ACKNOWLEDGEMENTS:

REFERENCES

[1] A. Manthiram, *Nat. Commun.*, **11**, 1550 (2020).

[2] S.-T. Myung, F. Maglia, K.-J. Park, C.S. Yoon, P. Lamp, S.-J. Kim, Y.-K. Sun. *ACS Energy Lett.*, **2**, 196 (2017).

[3] A. Kwade, W. Haselrieder, R. Leithoff, A. Modlinger, F. Dietrich, K. Droeder. *Nat. Energy*, **3**, 290 (2018).

[4] F. Pouraghajan, H. Knight, M. Wray, B. Mazzeo, R. Subbaraman, J. Chistensen, D. Wheeler. *J. Electrochem. Soc.*, **165**, A2644 (2018).

[5] T.M.M. Heenan, A. Wade, C. Tan, J.E. Parker, D. Matras, A.S. Leach, J.B. Robinson, A. Llewellyn, A. Dimitrijevic, R. Jervis, P.D. Quinn, D.J.L. Brett, P.R. Shearing. *Adv. Energy Mater.*, **10**, 2002655 (2020).

[6] C. Meyer, M. Kosfeld, W. Haselrieder, A. Kwade. *Journal of Energy Storage*, **18**, 371 (2018).

[7] E.N. Primo, M. Chouchane, M. Touzin, P. Vazquez, A.A. Franco. *J. Power Sources*, **488**, 229361 (2021).

[8] C. Meyer, M. Weyhe, W. Haselrieder, A. Kwade. *Energy Technol.*, **8**, 1900175 (2020).

[9] A.C. Ngandjong, T. Lombardo, E.N. Primo, M. Chouchane, A. Shodiev, O. Arcelus, A.A. Franco. *J. Power Sources*, **485**, 229320 (2021).

[10] J. Li, A.R. Cameron, H. Li, S. Glazier, D. Xiong, M. Chatzidakis, J. Allen, G.A. Botton, J.R. Dahn. *J. Electrochem. Soc.*, **164**, A1534 (2017).

[11] J. Li, H. Li, W. Stone, R. Weber, S. Hy, J.R. Dahn. *J. Electrochem. Soc.*, **164**, A3529 (2017).

[12] A. van Bommel, J.R. Dahn. *Electrochem. Solid-State Lett.*, **13**, A62 (2010).

[13] E. Trevisanello, R. Ruess, G. Conforto, F.H. Richter, J. Janek. *Adv. Energy Mater.*, **11**, 2003400 (2021).

[14] N. Yabuuchi, Y. Koyama, N. Nakayama, T. Ohzuku. *J. Electrochem. Soc.*, **152**, A1434 (2005).

[15] L.S. de Vasconcelos, N. Sharma, R. Xu, K. Zhao. *Exp. Mech.*, **59**, 337 (2019).

[16] D.J. Miller, C. Proff, J.G. Wen, D.P. Abraham, J. Bareño. *Adv. Energy Mater.*, **3** 1098 (2013).

[17] J.E. Harlow, X. Ma, J. Li, E. Logan, Y. Liu, N. Zhang, L. Ma, S.L. Glazier, M.M.E. Cormier, M. Genovese, S. Buteau, A. Cameron, J.E. Stark, J.R. Dahn. *J. Electrochem. Soc.*, **166**, A3031 (2019).

[18] K. Märker, P.J. Reeves, C. Xu, K.J. Griffith, C.P. Grey. *Chem. Mater.*, **31**, 2545 (2017).

[19] L. Feng, X. Lu, T. Zhao, S. Dillon. *J. Am. Ceram. Soc.*, **102**, 372 (2019).

[20] Y. Bi, J. Tao, Y. Wu, L. Li, Y. Xu, E. Hu, B. Wu, J. Hu, C. Wang, J-G. Zhang, Y. Qi, J. Xiao. *Science*, **370**, 1313 (2020).

[21] R. Xu, H. Sun, L.S. De Vasconcelos, K. Zhao. *J. Electrochem. Soc.*, **164**, A3333 (2017).

[22] R. Hill, *The Mathematical Theory of Plasticity*, Clarendon Press, Oxford (1950).

[23] X. Zheng, X. Li, B. Zhang, Z. Wang, H. Guo, Z. Huang, G. Yan, D. Wang, Y. Xu. *Ceram. Int.* **42**, 644 (2016).

[24] F.H. Allen, G. Bergerhoff, R. Sievers, *Crystallographic Databases*, International Union of Crystallography, Chester (1987).

[25] V. Marx, H. Balke. *Acta Mater*., **45**, 3791 (1997).

[26] A.K. Bhattacharya, W.D. Nix. *Int. J. Solids Struct*., **27**, 1047 (1991).

[27] D. Durban, N.A. Fleck. *J. Appl. Mech*., **59**, 706 (1992).

[28] A.E. Giannakopoulos, P.-L. Larsson, R. Vestergaard. *Int. J. Solids Struct*., **31**, 2679 (1994).

[29] A.K. Bhattacharya, W.D. Nix. *Int. J. Solids Struct*., **24**, 1287 (1988).

[30] M.F. Doerner, D.S. Gardner, W.D. Nix. *J. Mater. Res*., **1**, 845 (1986).

[31] M.W. Barsoum, M. Radovic. *Annu. Rev. Mater. Res.*, **41**, 195 (2011).

[32] M. Higashi, S. Momono, K. Kishida, N.L. Okamoto, H. Inui. *Acta Mater*., **161**, 161 (2018).

Deshpande and Fleck (2000). JMPS metal foam paper.

Johnson, K.L Contact mechanics, CUP…..

FIGURES AND TABLES

(a)

(b)
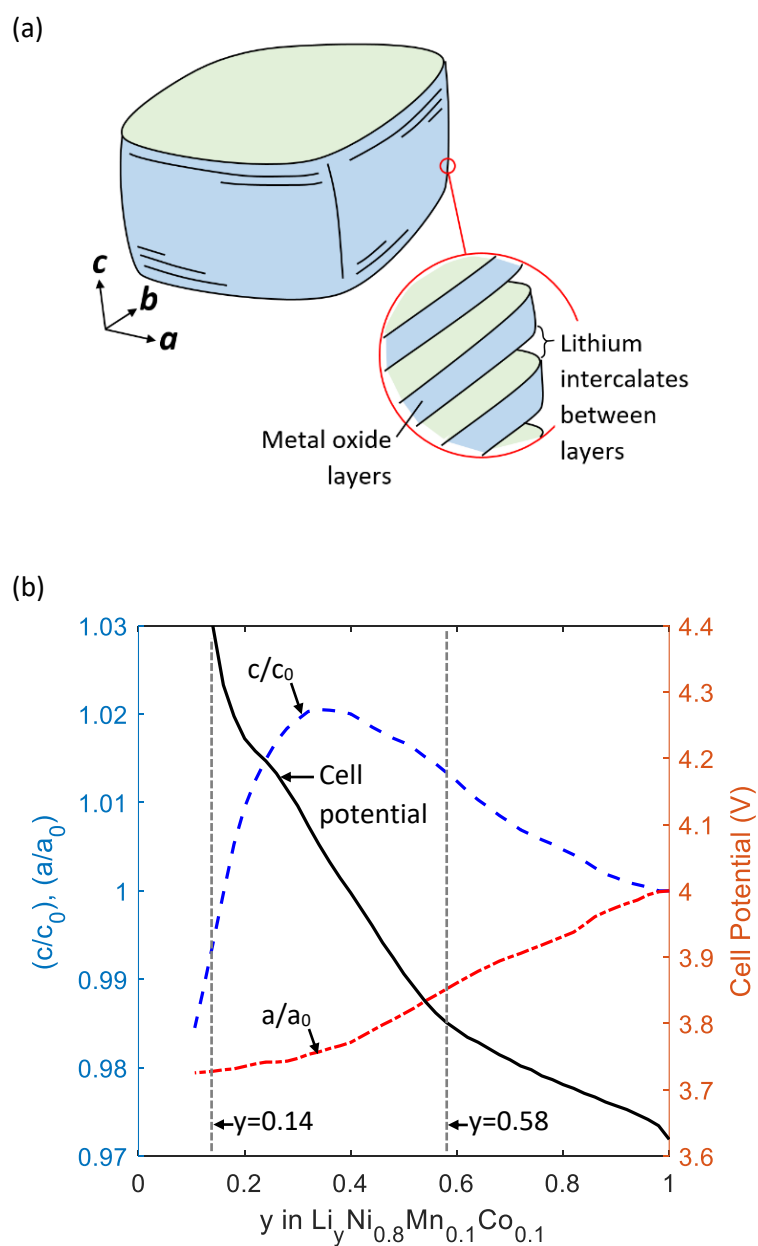
Figure 1: (a) Sketch of an NMC811 single crystal, illustrating the prismatic direction c and the layered atomic structure. (b) Sensitivity of the normalised unit cell dimensions a/a_0 and c/c_0 and cell potential to lithium content y for single crystal NMC811 cathodes during the first charge at 10 mAh g^{-1}, as reported elsewhere [18].

(a)

(b)

Slip

5 µm

1 µm

(c)

Fracture

1 µm
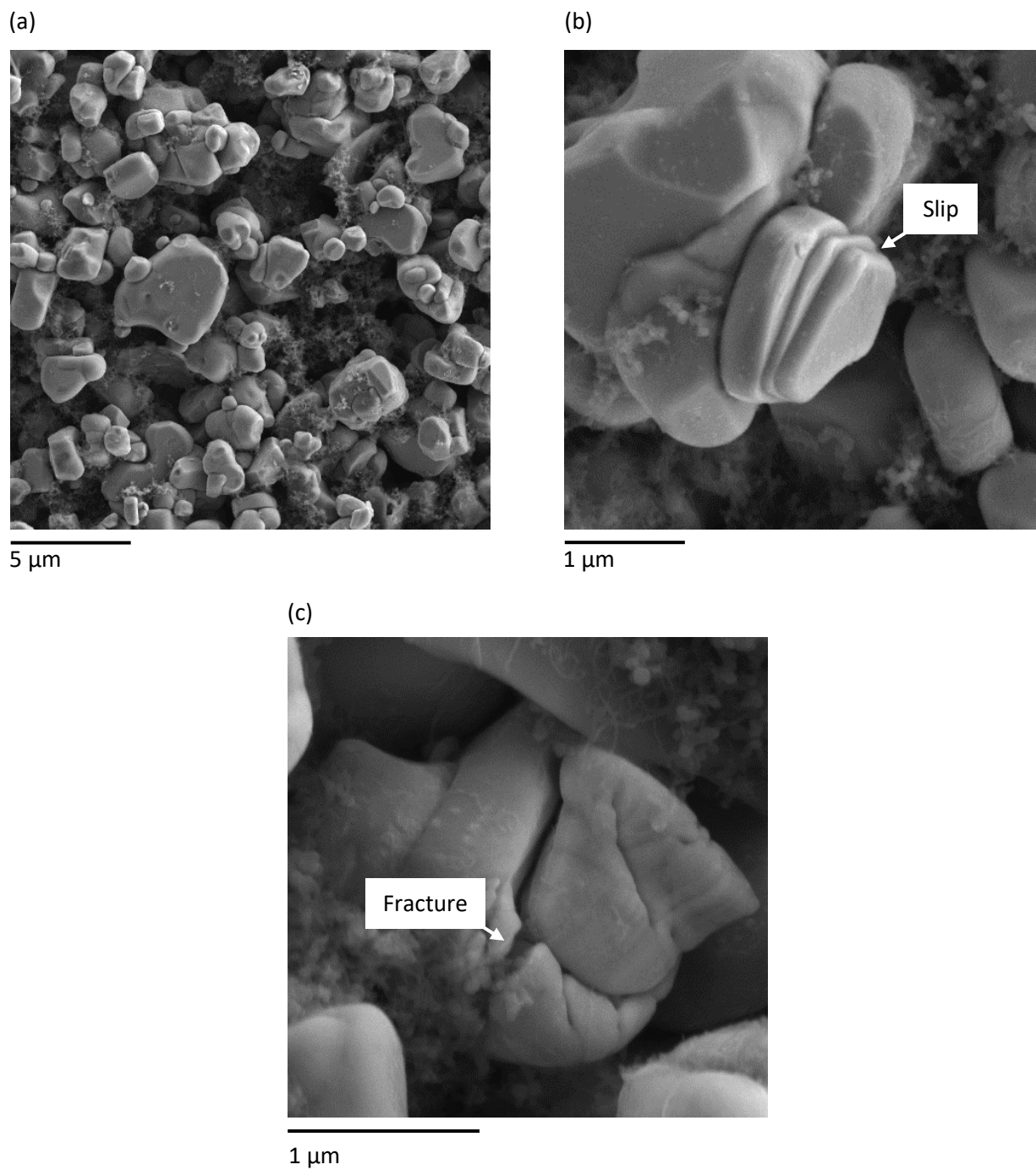
Figure 2: Images of individual single crystal cathodes particles obtained with a scanning electron microscope: (a) the microstructure of a fully lithiated ($y = 1$) single-crystal NMC811 cathode in plan view. Single crystal cathode particles with evidence of (b) slip planes and (c) fracture.
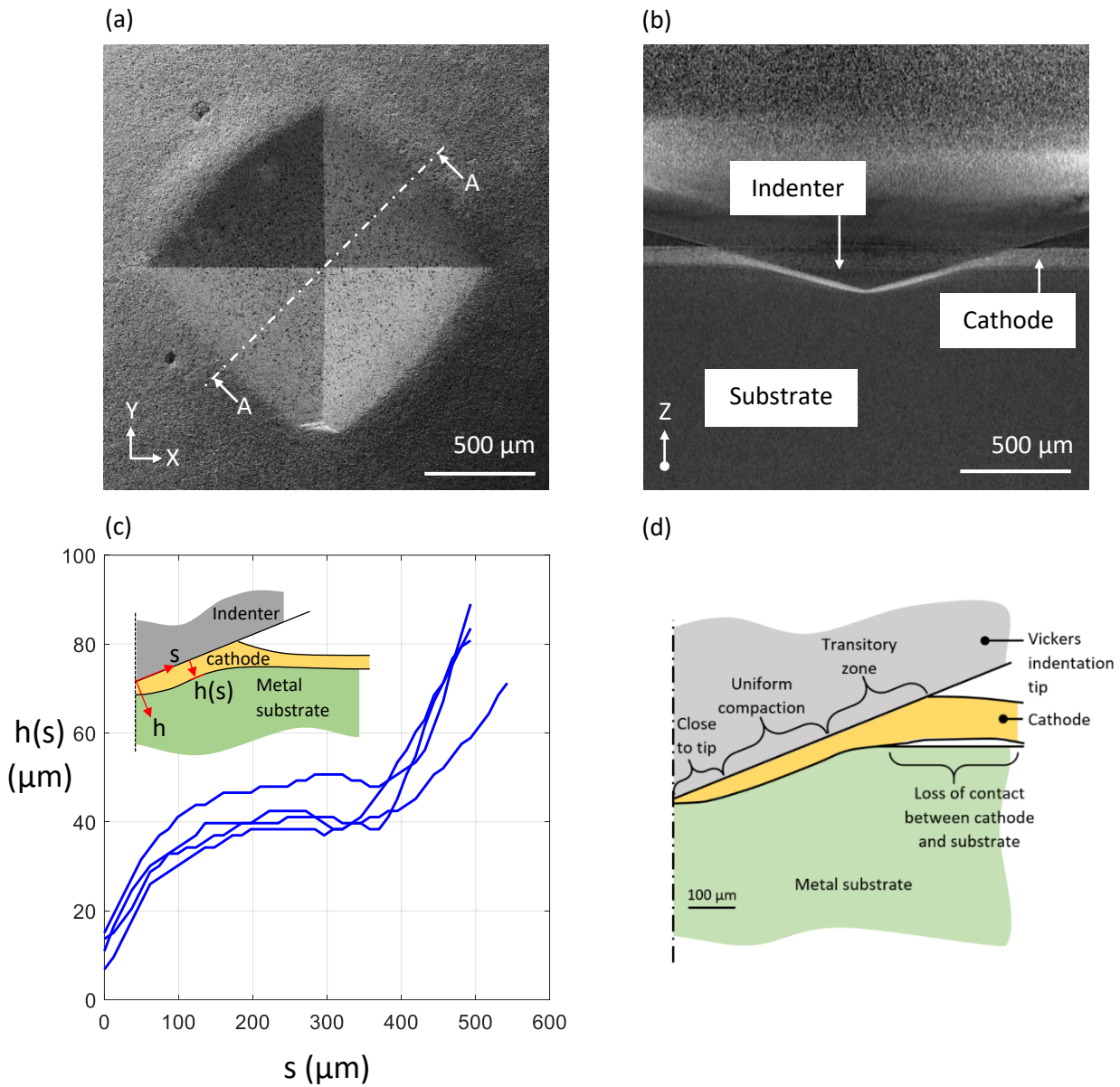
Figure 3: (a) Image of a fully lithiated (y = 1) cathode after indentation by a load of 120 N load upon an annealed aluminium substrate. (b) Image of the cathode during indentation, along the cross section A-A, as identified in (a). (c) Plot of cathode thickness measured perpendicular to the indenter flank as a function of distances from the tip, and (d) zones of deformation of the cathode. Image (b) and the plots (c) and (d) are obtained from in-situ X-ray computed tomography at a fixed load of 120 N.
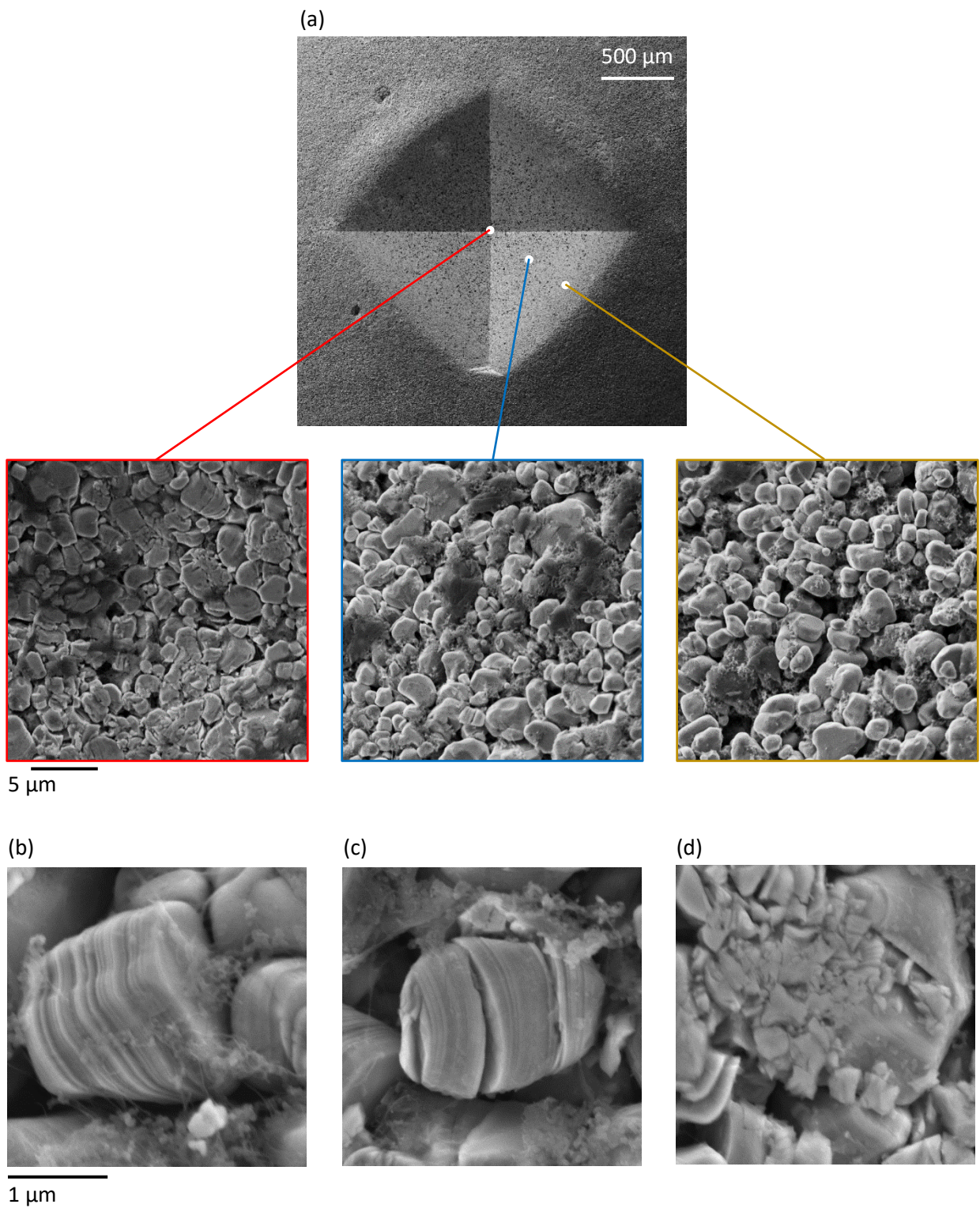
Figure 4: (a) Variation in the degree of compaction within an indent of a fully lithiated ($y = 1$) cathode. Images of (b) particles with slip bands, and (c)-(d) of particles with various combinations of slip bands and fracture.

(a) As-received cathode
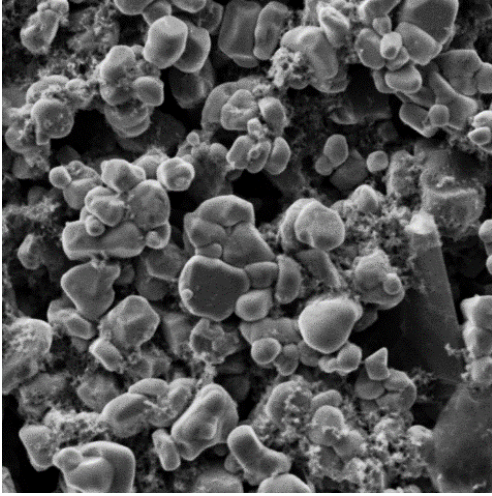
(b) Sn-Cu Alloy: H=127 MPa
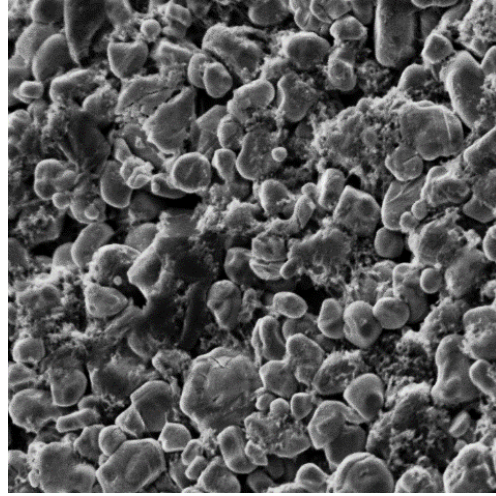
(c) As-received Al: H=406 MPa
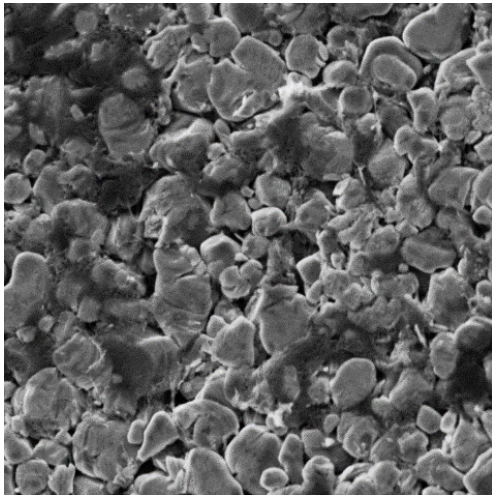
(d) As-received Cu: H=946 MPa
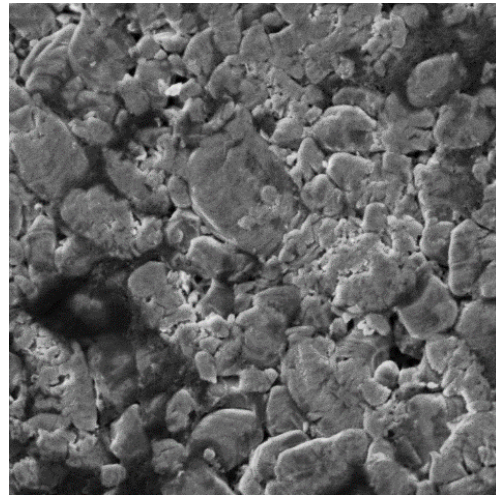
5 µm

Figure 5: Microstructure of the as-received, fully lithiated ($y = 1$) cathode (a) and indented cathodes (b)-(d) imaged after indentation upon substrates of increasing hardness. Images of the indented cathode are obtained at a distance of $\sqrt{A_P}/4$ from the apex of each indent and equidistant between two edges. All images are obtained by SEM.
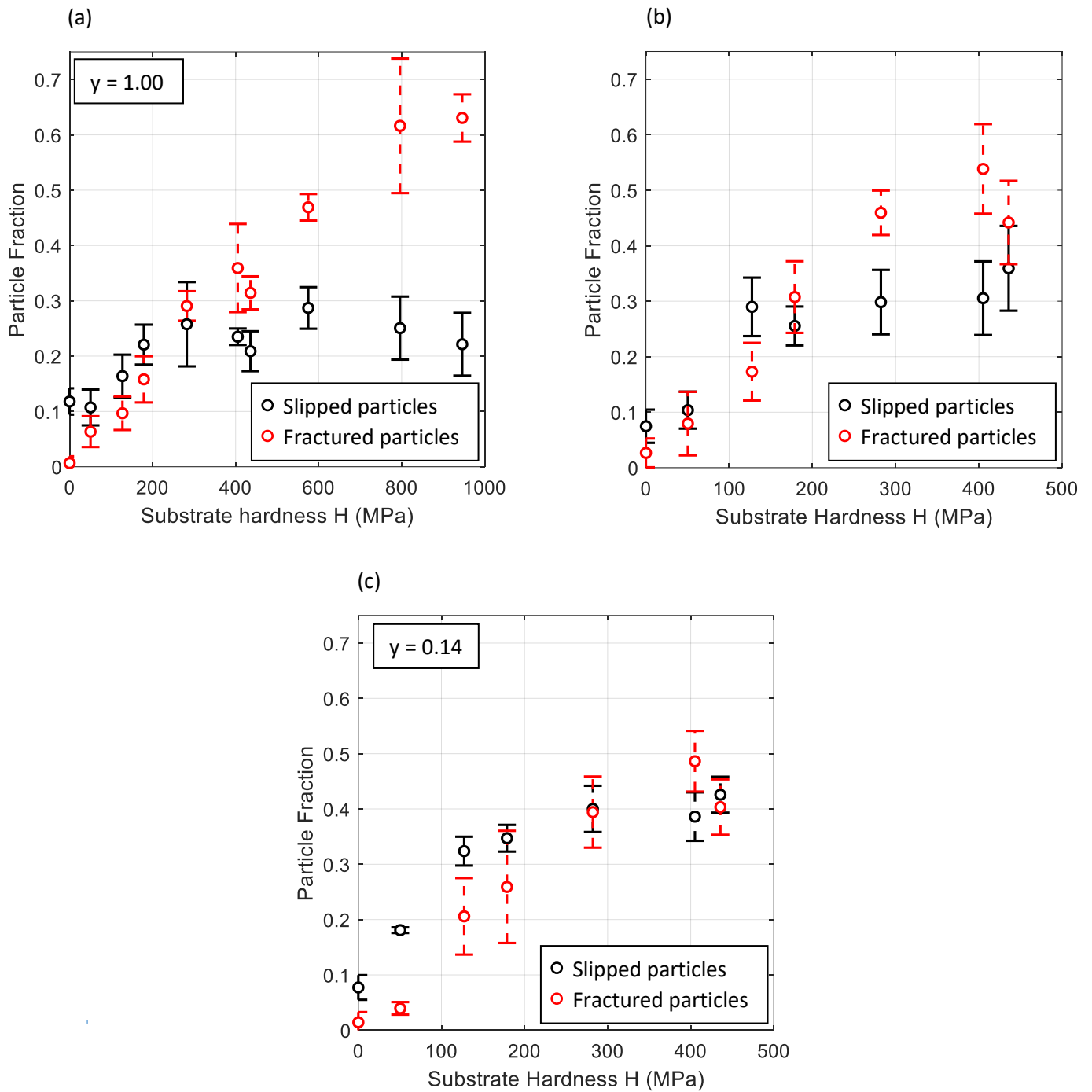
Figure 6: The mean fraction of particles with slip bands and fractures counted from images of the indented cathode microstructure are plotted against the substrate hardness H for a lithium occupancy of (a) $y = 1.00$; (b) 0.58 and (c) 0.14. Bars are included in the plotted data represent one standard deviation from the mean number fractions.
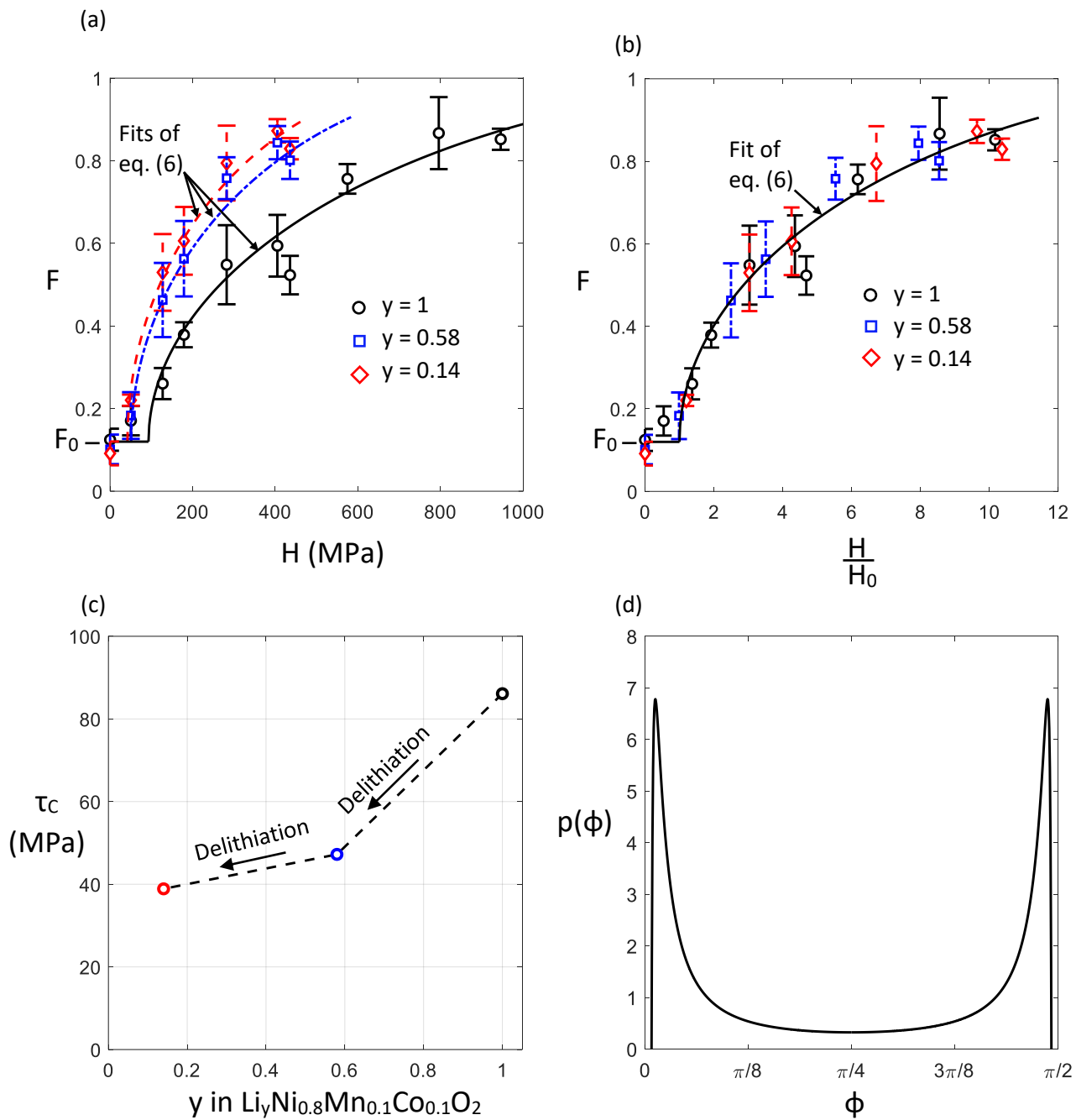
Figure 7: The measured cumulative fraction of slipped particles versus (a) substrate hardness H, and (b) versus normalised substrate hardness H/H_0. (c) Average basal shear strength versus degree of lithiation as deduced from the slip model. (d) The orientation function of particles within the cathode $p(\phi)$ as deduced from the fit for $F(H/H_0)$.
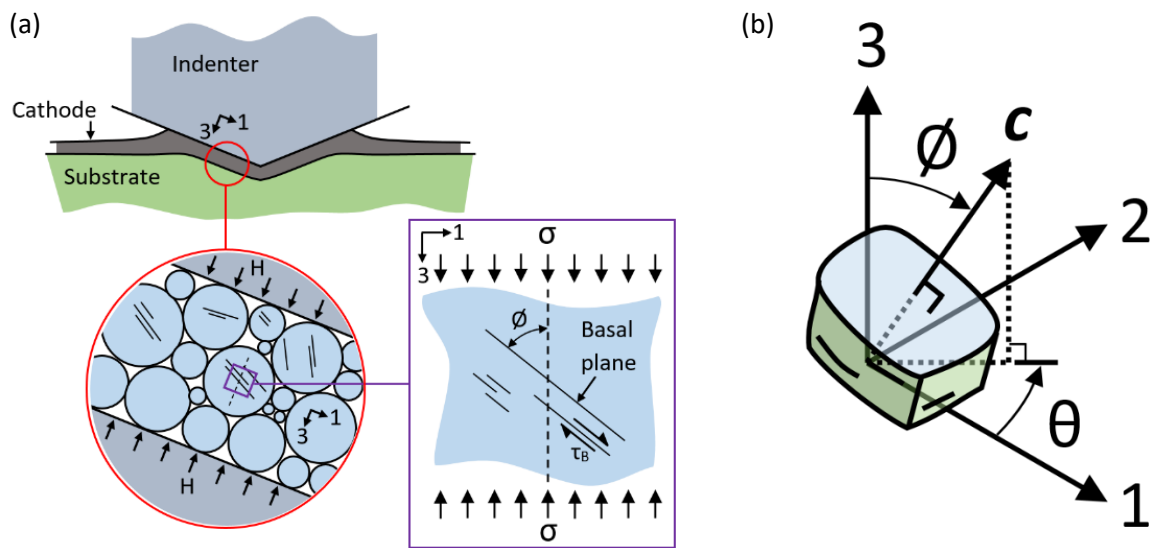
Figure 8: (a) Sketch of the cathode during indentation, with stresses at the cathode and particle level annotated. (b) The unit normal to the basal plane c, and the angle of basal plane inclination ϕ are relative to the 3-direction along which compressive tractions are applied in the indentation tests.

SUPPLEMENTARY INFORMATION

TABLE S1: The composition, preparation and Vickers hardness of the metal substrates used in cathode indentation testing.

Metal	Composition and origin.	Heat treatment and degree of work hardening	Measured hardness H (MPa)
Lead	99.9 % Pb by mass, obtained from Alfa Aesar UK[10].	No heat treatment or work hardening.	50.4
Tin-Copper Alloy	Nominal composition Sn 99%, Cu 1% by mass. Manufactured by Stannol GMBH [11]	No heat treatment or work hardening.	127
Annealed Aluminium 1080 A	Al >99.8% by wt. Source metal obtained from Aalco Metals Ltd. [12]	Annealed at 400°C for 1 h, then cooled in air.	179
Annealed Aluminium 1080 B		Annealed at 343°C for 1 h, then cooled in air.	283
Aluminium 1080 as-received		No heat treatment.	406
Annealed copper	Cu > 99.9% by wt. Grade Copper C101, obtained from Aalco metals Ltd.	Annealed at 400°C for 2 h, then cooled in air.	436
Annealed and work hardened copper A		Annealed at 400°C for 2 h, then cooled in air, and work hardened in compression to a true stress of 100 MPa.	575
Annealed and work hardened copper B		Annealed at 400°C for 2 h, then cooled in air, and work hardened in compression to a true stress of 200 MPa.	796
Copper in as-received condition		No heat treatment or work hardening.	946

[10] 00930.KF Lead bar. Obtained from Alfa Aesar, Shore Rd., Port of Heysham Industrial Park, Lancashire, LA3 2XY, United Kingdom.
[11] Lead Free Solder Bar (99% Sn, 1% Cu) 1 1kg. Manufactured by Stannol GMBH & CO. KG., Haberstr. 24, D-42551 Velbert, Germany.
[12] Aalco metals Ltd., Parkway House, Unit 6 Parkway Industrial Estate, Pacific Avenue, Wednesbury, West Midlands, WS10 7WP, United Kingdom.